Article

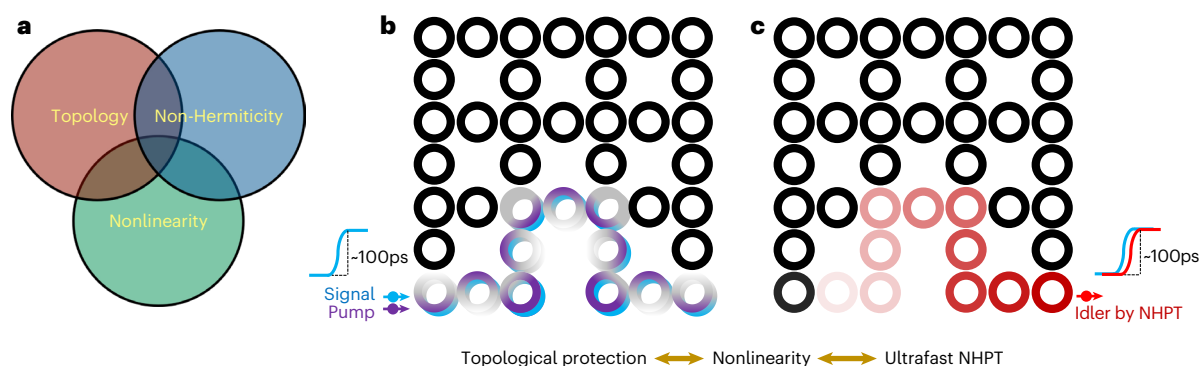# Non-Hermitian topological phase transitions controlled by nonlinearity

Tianxiang Dai [1], Yutian Ao[1], Jun Mao [1], Yan Yang [2], Yun Zheng[1], Chonghao Zhai[1], Yandong Li[1], Jingze Yuan [1], Bo Tang[2], Zhihua Li [2], Jun Luo[2], Wenwu Wang[2], Xiaoyong Hu [1,3,4,5,6], Qihuang Gong [1,3,4,5,6] & Jianwei Wang [1,3,4,5,6] ✉

Manipulating topological invariants is possible by modifying the global properties of optical devices to alter their band structures. This could be achieved by statically altering devices or dynamically reconfiguring devices with considerably different geometric parameters, even though it inhibits switching speed. Recently, optical nonlinearity has emerged as a tool for tailoring topological and non-Hermitian (NH) properties, promising fast manipulation of topological phases. In this work, we observe topologically protected NH phase transitions driven by optical nonlinearity in a silicon nanophotonic Floquet topological insulator. The phase transition occurs from forbidden bandgaps to NH conducting edge modes, which emerge at a nonlinearity-induced gain–loss junction along the boundaries of a topological insulator. We find static NH edge modes and dynamic phase transitions involving exceptional points at a speed of hundreds of picoseconds, which inherently retain topological protections against fabrication imperfections. This work shows an interplay between topology and non-Hermiticity by means of nonlinear optics, and it provides a way of manipulating multiple phase transitions at high speeds that is applicable to many other materials with strong nonlinearities, which could promote the development of unconventionally robust light-controlled devices for classical and quantum applications.

The physics of topology, which originated from quantum materials in condensed matter[1], allows the development of topologically protected photonic devices that are immune to disorders and defects[2–6]. Photonic topological edge states with broken time-reversal symmetry were first observed in a gyromagnetic photonic crystal[3], and various topological non-trivial phases have been observed in non-magnetic optical devices with different configurations, such as waveguide arrays[7,8], microring lattices[9,10] and photonic crystals[11,12]. Going beyond condensed matter systems, photonic topological systems, which incorporate

highly controllable non-Hermiticity and nonlinearity, could provide a versatile platform for experimental investigation of topological phenomena and the development of unconventional photonic devices. Recently, an emerging interplay of topological photonics[2–6] and non-Hermitian (NH) photonics[13–16] has exhibited an interesting synergy among multiple phases and phase transitions[17–19]. Enriched by the non-Hermiticity, it has enabled the realizations of topological lasers[20], topological photon-pair sources[21,22], topological entangled-photon emitters[23], topological parity-time symmetric crystals[24], NH topological

[1]State Key Laboratory for Mesoscopic Physics, School of Physics, Peking University, Beijing, China. [2]Institute of Microelectronics, Chinese Academy of Sciences, Beijing, China. [3]Frontiers Science Center for Nano-optoelectronics & Collaborative Innovation Center of Quantum Matter, Peking University, Beijing, China. [4]Collaborative Innovation Center of Extreme Optics, Shanxi University, Taiyuan, China. [5]Peking University Yangtze Delta Institute of Optoelectronics, Nantong, China. [6]Hefei National Laboratory, Hefei, China. ✉e-mail: jww@pku.edu.cn

Fig. 1 | Nonlinearity-driven NH phase transitions in a photonic FTI. a, An interplay of topological photonics, NH photonics and nonlinear photonics. The FTI works in a triply intersected regime, in which topology and non-Hermiticity interact by means of the FWM. **b,c**, An illustration of light field distributions. As an example, the FTI consists of a two-dimensional lattice of four-by-four main site rings, where one link ring is removed to show topological immunity to imperfections. The FTI is fabricated on silicon nanophotonic waveguides with a strong FWM effect. In **b**, the externally input pump and signal light are excited in the topological non-trivial edge modes in the AFTI phase. The idler light, if externally injected, is in the forbidden bandgaps in the CI phase and transport is prohibited. The topological phase transition from the AFTI phase to the CI phase is steered by the wavelength of the light. Creating a gain–loss junction at the edge of topological insulators, where gain is induced by nonlinearity on the edge and loss is induced by dissipation into the bulk, results in the NHPT of the idler. In contrast with the externally input idler light that was prohibited, the internally FWM-generated idler light can be transported on the NH edges, as shown in **c**. The unique property of topological protections is inherited from the externally input pump and/or signal light in the topological edge modes (**b**) to the internally generated idler light in the NH edge modes (**c**). The interplay of topology and non-Hermiticity by means of FWM harmoniously synthesizes the capabilities of fast NHPT and topological protections.

steering of light[18], observation of NH bulk-boundary correspondence[25] and the generation of arbitrary topological windings of an NH band[26]. Moreover, optical nonlinearities that are highly controllable and exist naturally in almost all optical materials, have shown the potential to provide a general and practical tool for controlling new topological photonic devices. For example, the harnessing of nonlinearities[27,28] has enabled the operation of nonlinearity-induced topological insulators[29–32], Floquet solitons[33] and topological quantum light sources[21–23]. Non-Hermiticity can also be well tailored by engineering loss and gain from nonlinear effects[13–16,34–36]. Figure 1a illustrates an interplay between topology, non-Hermiticity and nonlinearity, by which sophisticated properties of band structures can be engineered for unconventional photonic devices. Previous work has mostly focused on paired interactions between topology, non-Hermiticity and nonlinearity, whereas a triple interplay among them may lead to new findings. For example, it has recently allowed tuning of parity-time symmetry and non-Hermiticity in a topological insulator using self-focusing and defocusing effects[37].

Fast switching and reconfiguring of topological photonic states represents a key enabling capability. At the fundamental level, it could provide a means of understanding the dynamics of emergence and transition of topological phases, to reveal collective phenomena, create correlated states of light and probe the limits of how fast topological systems can operate. It could also provide robust photonic devices for practical applications, such as optical routing, modulation, isolation, amplification and frequency conversion for optical information processing, telecommunications and interconnection[38], and quantum information processing and communication[39]. The transformation of topological phases could be achieved by statically replacing devices[4–7], dynamically altering the global geometric parameters of the devices[40–42] or flexibly patterning the pumping light fields[18]. The switching or reconfiguring time is expected to be of the order of milliseconds to seconds using these dynamic approaches. Fast switching of topological phases remains challenging. Several theoretical proposals[43,44] and experimental demonstrations (in the microwave domain)[45] for fast switching of topological phases of the order of nanoseconds have been reported, which are still far away from those achieved in conventional photonic devices.

In this work, we observe nonlinearity-driven fast NH phase transitions involving exceptional points in a photonic Floquet topological insulator (FTI) on a silicon chip. By harnessing the four-wave mixing (FWM) nonlinearity of silicon nanowaveguides to engineer band structures, light that was in a forbidden bandgap can now be transported along a topological gain–loss junction at which an NH phase transition (NHPT) occurs. We measured an NHPT speed of about 250 ps and show that its dynamics can be topologically protected against imperfections. Coherence of the NH edge modes is explicitly confirmed by implementing interferometric measurements. Our device can be operated with a fast speed comparable with that in conventional photonic devices, but featuring topological robustness. Our approach could apply to many other optical materials with strong nonlinearities. Generally, an interplay of topology and non-Hermiticity by means of nonlinearity could provide a highly engineerable platform for fundamental research and the development of new photonic devices.

The FTI in a two-dimensional lattice of coupled microrings can be realized in the absence of a magnetic field by the periodic evolution of light in the microrings, emulating a periodically driven Hamiltonian[46–49]. As shown in Fig. 1b,c, the device consists of a square lattice of microrings supporting two degenerate counterpropagating pseudospins. The topology of band structures of Floquet devices is fully determined by the coupling strength (θ) between neighbouring microrings linked by evanescent directional couplers (DCs) with an amplitude reflectance of $\cos\theta$ and transmittance of $\sin\theta$. All microrings and their coupling configurations are designed identically, which is different from the photonic quantum Hall insulators with an effective gauge field emulated by offset rings[9,10]. The FTI is described by a Floquet model of $\mathcal{U}_F(\theta, k) |\psi\rangle = e^{-i\epsilon T} |\psi\rangle$, where $\mathcal{U}_F(\theta, k)$ is the Floquet transfer matrix of θ and the Bloch wavevector k operating on the eigenstate $|\psi\rangle$, ϵ is the quasi-energy and T is one period of evolution[48,49]. The matrix can be regarded as a time-evolution operator, that is, $\mathcal{U}_F(\theta, k) = \mathcal{T} \exp[-i \int_0^T H_k(\theta, t) \, dt]$, where $\mathcal{T}$ is the time ordering. We get an effective Hamiltonian as $\mathcal{H}_{eff}(\theta, k) = i \ln(U_F(\theta, k))/T$.

The FTI works in a linear or a nonlinear regime when the parametric gain from FWM (inducing non-Hermiticity) is absent or present, respectively. Figure 2a–c shows the calculated Riemann sheet and band structures for an FTI in the linear regime with no gain. The calculated
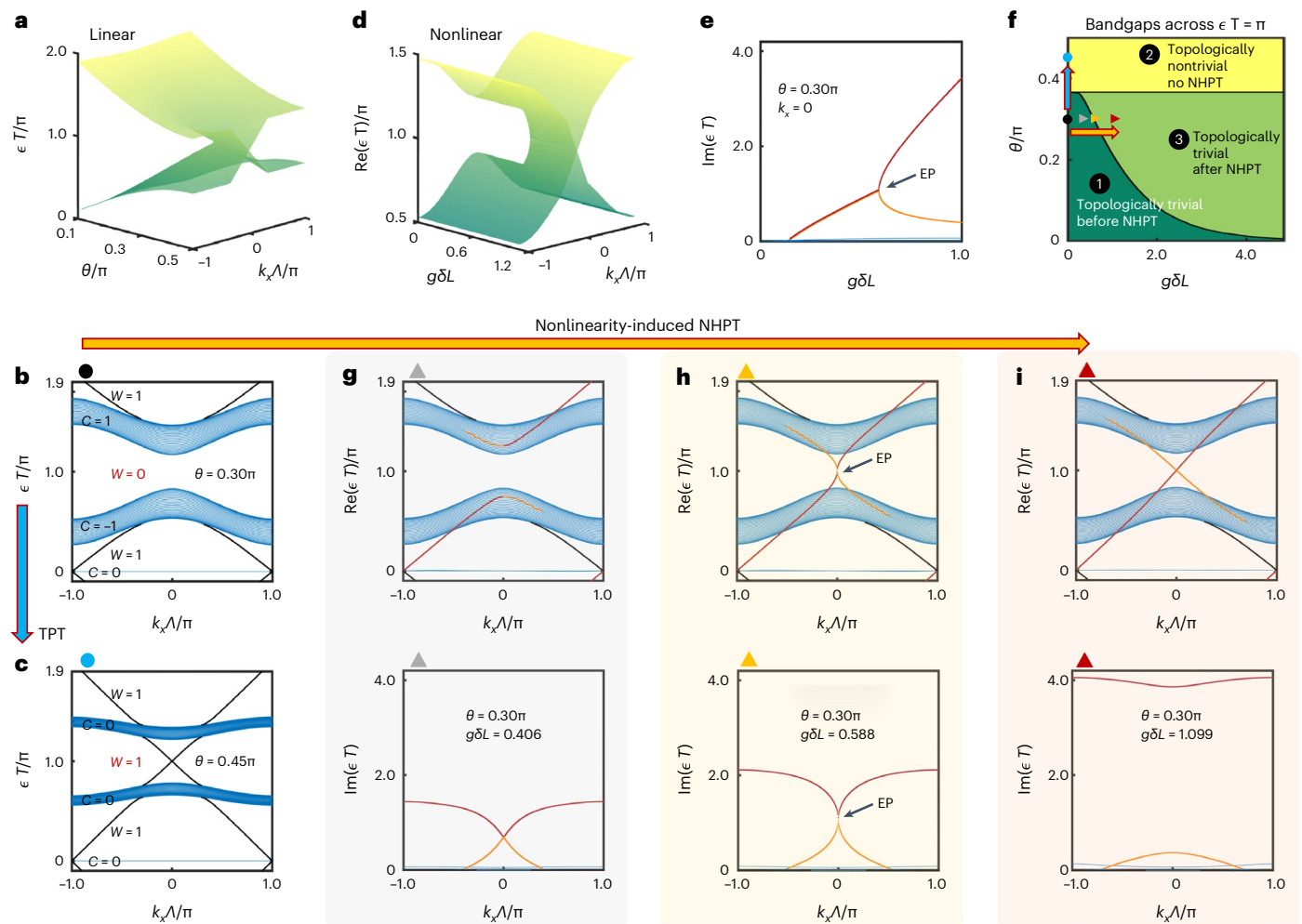
Fig. 2 | Calculated band structures and phase diagram of the FTI in linear and nonlinear regimes. a, The Riemann sheet of the eigenspectrum for different coupling strength θ and momentum k_x (Λ is the period of the lattice), when setting the gain as $g\delta L = 0$. **b,c**, Projected band structures for the CI phase ($\theta = 0.3\pi$) and AFTI phase ($\theta = 0.45\pi$). In **a**–**c**, they describe the closing and reopening of bandgaps at $\epsilon = \pi/T$ during the TPT process (blue arrow) in the linear FTI. **d**, The Riemann sheet of the real part of the eigenspectrum for different values of gain coefficient $g\delta L$ and momentum k_x, when setting the coupling strength as $\theta = 0.3\pi$ in the CI phase. **e**, The imaginary part of the band structure projected onto the $k_x = 0$ plane, which shows the mode splitting at the EP, as the boundary gain increases. **d,e** show the exceptional point and NHPT process in the

nonlinear FTI. **f**, The complete phase diagram of TPT and NHPT for the bandgap across $\epsilon = \pi/T$. It consists of three regimes: (1) topologically trivial, before NHPT (under the critical points of TPT and NHPT); (2) topologically non-trivial without NHPT (above the TPT point); (3) topologically trivial, after NHPT (above the EP point of NHPT). Coloured symbols in the $\{\theta, g\delta L\}$ diagram refer to examples before and after the phase transitions in **b,c** and **g**–**i**. **g**–**i**, Band structures for $g\delta L = 0.406$, 0.588 and 1.099 ($\theta = 0.3\pi$), respectively, which describe the closing and reopening of bandgaps at $\epsilon = \pi/T$ in the NTPT (yellow arrow). Topological edge modes are indicated by black lines in **b,c** and NH edge modes are highlighted by red and orange lines in **g**–**i**. The real parts of the band structures are plotted in a shifted window of $[-0.1\pi, 1.9\pi]$ to show a narrow bulk band at $\epsilon = 0$.

Chern numbers ($\mathcal{C}$) and winding number ($\mathcal{W}$) are indicated in the band structures. When the coupling strength of θ is greater than $\arccos(\sqrt{2} - 1)$, the lattice works in a strongly coupled regime and the topological non-trivial edge modes emerge at the bandgaps across $\epsilon = \pi/T$, resulting in the anomalous Floquet topological insulator (AFTI) phase. Figure 1b shows meandering edge modes in real space and Fig. 2c shows three pairs of edge modes at $\epsilon = 0_\pm$ and π/T in momentum space. Otherwise, as the coupling strength is gradually reduced down to the critical point, the bandgap across $\epsilon = \pi/T$ opens, resulting in the Chern insulator (CI) phase (Fig. 2b). Tailoring the coupling of DCs thus results in the topological phase transition (TPT) between CI and AFTI and it enables the changing of the topology of bandgaps across $\epsilon = \pi/T$ between trivial and non-trivial phases. In addition, the edge states at $\epsilon = 0_\pm$ always exist. A full phase diagram for the FTI in the linear regime is plotted in Supplementary Fig. 3d and details are provided in the Supplementary Information.

Figure 3a shows the measured transmission spectrum of the FTI device in the linear regime. We fabricated a device with six-by-six main site rings, as shown in Fig. 3b. Fabrication details are provided in the Supplementary Information. High transmission is observed in the FTI, due to its strong coupling between sites, which makes it well suited for all classical optical and quantum applications. In our experiment, the TPT from the CI phases (Fig. 3c) to the AFTI phases (Fig. 3e) occurs when reducing the wavelength (λ) of light from 1,580 nm to 1,510 nm[8,50]. This is because of the smaller difference in the wavevectors between the symmetrical and antisymmetrical supermodes of the DCs at the shorter wavelength. As shown in Fig. 3c, within one free spectral range (FSR), there are three edge states (broad flat plateaux) separated by bulk states (fluctuated dissipated dips). With the decrease in wavelength, the coupling strength gradually becomes weaker, leading to the disappearance of the edge mode sandwiched between two bulk modes and giving rise to a new forbidden bandgap, as shown in Fig. 3e.
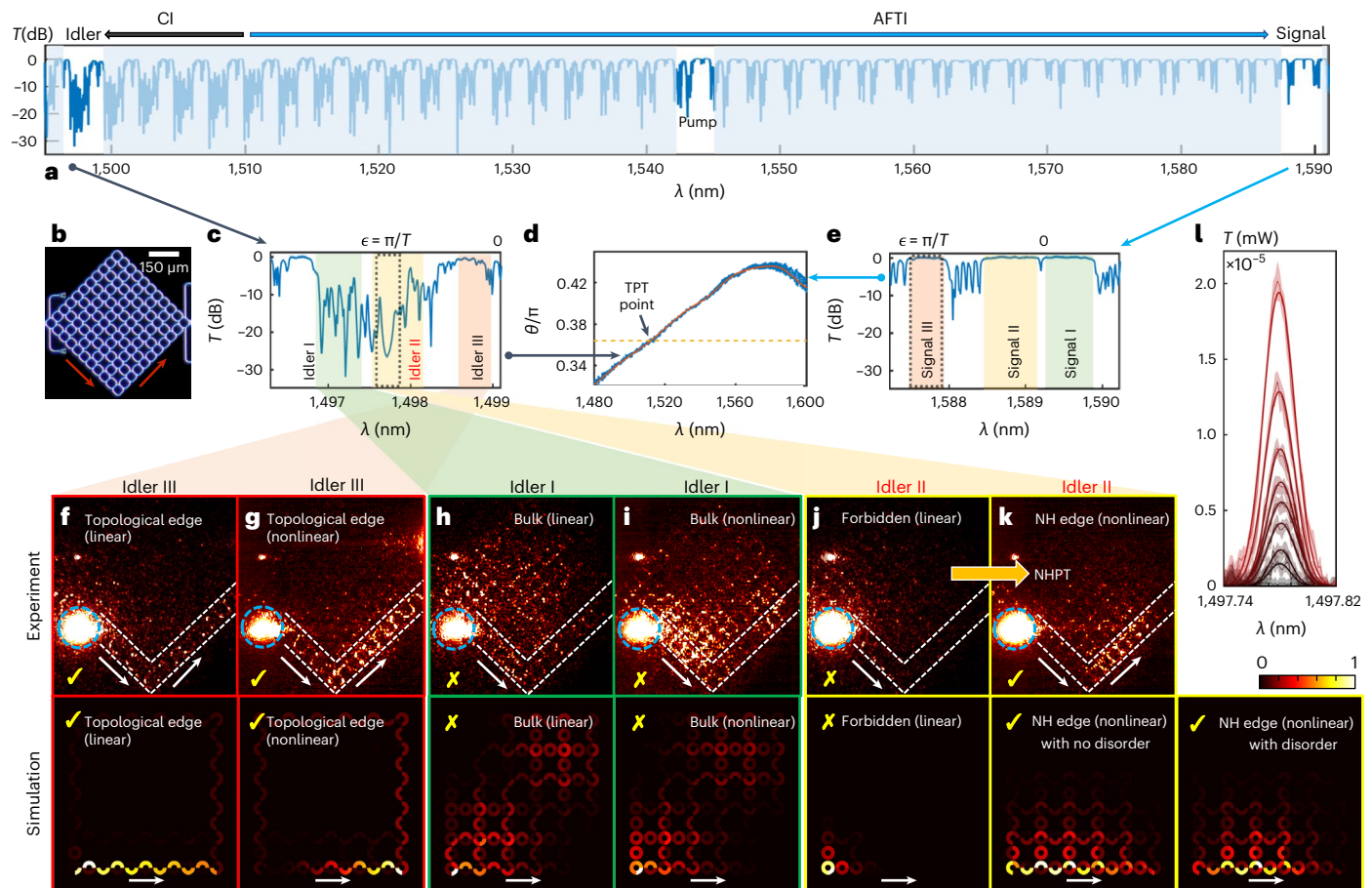
Fig. 3 | Experimental results of topological and NH phase transitions.
a, Measured linear transmission spectrum of the fabricated FTI device in **b**.
Wavelengths for the pump, signal and idler light in our experiments are indicated
in white windows, respectively. Spectra regions for the AFTI and CI phases
are shown. **b**, Optical microscopy image of the fabricated FTI. **c**,**e**, Zoomed-in
views of the one-FSR spectrum for the idler (**c**) and signal (**e**) light in the CI and
AFTI phases, respectively. The signal is chosen in the windows of {signal I, II, III},
whereas the idler is correspondingly given by the energy conservation and is
labelled in the windows of {idler I, II, III} for a fixed pump light at the wavelength
of 1542.0 nm. The bandgaps across $\epsilon = \pi/T$ of interest are boxed by grey dashed
lines. **d**, Measured spectral response of coupling strength θ for a DC. Points are
experimental data and the solid line shows theoretical data. The yellow dashed
line indicates the critical point of the TPT. **f**–**k**, Measured (top) and simulated
(bottom) real-space distributions of electromagnetic field in the FTI (the same
fabricated FTI in **b**) in topological edge modes (**f**), bulk modes (**h**), forbidden
bandgaps (**j**) with externally input idler light (in the linear regime) and topological
edge modes (**g**), bulk modes (**i**), NH edge modes (**k**) with internally FWM-

generated idler (in the nonlinear regime). The key result is shown in **k**: the NHPT
takes place from the forbidden bandgap in **j** to the NH edge mode in **k** by means of
nonlinear optics. In **k**, it shows the simulated light field for an FTI with and without
disorders in phase and coupling strengths. Dashed white lines are provided as
guides for the eye. Bright spots in blue circles indicate the out-of-plane diffracted
light from grating couplers (used for device characterizations). White arrows
indicate the light propagation directions. Simulation results for a larger lattice
are provided in Supplementary Fig. 6. **i**, Quantitative characterizations of the
NH edge mode. The spectral distributions for the generated idler light at the
forbidden bandgap are recorded when the pump and signal light are fixed at
specific wavelengths. Narrow spectral distributions appear, owing to the use of a
narrow linewidth pump and signal light. Optical intensity of the FWM-generated
idler at the gain–loss junction is detected, with an increase in the power of the
external signal light from 0.5 dB m to 14.5 dB m with an interval of 2 dB m. The
background noise around $T = 0$ mW represents the case with no signal input.
Shaded areas refer to mean intensity ±1 standard deviation (s.d.) from six
independent measurements and the solid lines are their Gaussian fitting.

That is, the TPT occurs by directly switching the wavelength of light
from longer to the shorter (indicated by two dashed boxes in Fig. 3c,e),
across the critical point shown in Fig. 3d. Figure 3f,h,j shows infrared
imaging of real-space distributions of electromagnetic fields in the
FTI in the linear regime when choosing the excitation wavelengths
of externally input light in the edge mode, forbidden bandgap and
bulk mode, respectively. Measured field distributions are consistent
with simulated results (bottom panels; see simulation model in
Supplementary Section 3).

The steering of gain and loss in optical devices allows the manipula-
tion of parity-time symmetry and NH phases[13–16]. Here, we harness the
intrinsic strong nonlinearity of fully passive silicon nanowaveguides,
that is, the FWM, to induce gains and impose the NHPT in FTI devices. By
means of the non-degenerate FWM, two pump photons at the frequency

of ω_{pump} are converted to signal and idler photons at the frequencies
of ω_{signal} and ω_{idler}, which satisfies energy conservation. In silicon
nanowaveguides with a cross-section of 450 nm × 220 nm, nonlinear
phase-matching is satisfied[51]. This leads to the nonlinearity-induced
amplification of light, which can be precisely controlled by nonlinear
optical technologies[27]. Importantly, when the externally injected
pump light and signal light (both at the long wavelengths, above the
TPT point) are selected to simultaneously excite the topological edge
modes in the non-trivial phase and they co-travel along the 'S'-shape
boundary (Fig. 1b; see the formation of the 'S'-shape in Supplementary
Fig. 2), the idler light (at the short wavelength, under the TPT point) that
was in the trivial bandgap, will be generated by FWM and is continuously
amplified as it goes by the overlapped paths. This results in the emer-
gence of a nonlinearity controlled gain–loss junction along boundaries.
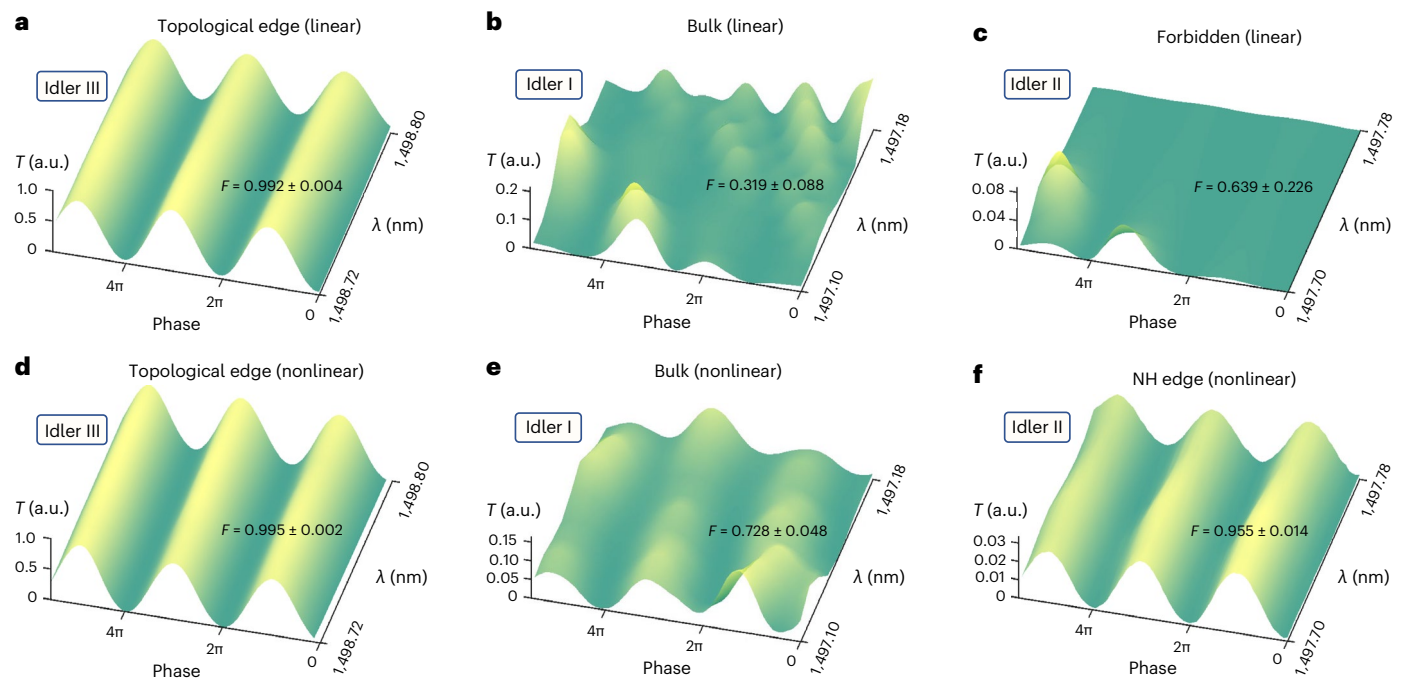
Fig. 4 | Probing coherence of topological non-trivial edge and NH edge modes. a–f, Optical interferometric measurements are implemented between two topological and NH edge modes, respectively. The FTI is embedded inside a Mach–Zehnder interferometer, in which the two arms are formed by two counterpropagating modes of the FTI. **a–c**, The relative phase between the two arms is operated by an integrated phase shifter. In the linear regime, an idler light is externally injected into the FTI to equally excite the clockwise and counterclockwise modes, and interference fringes of the two idler beams are measured when the device works in different phases: topological edge mode (**a**); bulk mode (**b**); and forbidden bandgaps (**c**). **d–f**, In the nonlinear regime, the pump light and signal light are together injected into the FTI to equally excite the clockwise and counter-clockwise modes, and interference fringes of the two FWM internally generated idler beams are measured when the device works in different phases: topological edge mode (**d**); bulk mode (**e**); and NH edge mode (**f**). To fully portray coherence, a group of interference fringes in the windows of {idler I, II, III} with a 0.01 nm step of wavelength (λ) are measured. a.u. indicates the interference fringes plotted in **b**,**d** and **e**,**f** are normalized to the maximum intensity of **a**,**d**, respectively. Classical statistic fidelity (F) is used to characterize the fringes, defined as $(\sum_i p_i \cdot q_i / (\| p \| \cdot \| q \|))^2$, where $p_i(q_i)$ is the measured (ideal) probability and $\|p(q)\|$ represents the Euclidean norm. The averaged values of F (with ±1 s.d. calculated from all sampling wavelengths) of all fringes in the windows of {idler I, II, III} are shown in the subplots.

Differently to the linear FTI, the above model has to be modified with an inclusion of gain and loss in the nonlinear regime. The gain can be described by a factor of ($g_{x,y}L$), where $g_{x,y}$ is a gain coefficient that is inhomogeneously position dependent and L is the propagation length of the light. To show the evolution of band structures in the NHPT, we simplify the gain map, assuming that $g_{x,y} = g$ for the 'S'-shaped paths of the topological edge modes and $g_{x,y} = 0$ for the bulk region. The loss that competes with the boundary gain is determined by the dissipation into the bulk lattice (see simulations in Supplementary Fig. 6), which can be controlled and quantified by the coupling strength of the lattice. Note that we assume that the propagation loss is globally uniform in the lattice so that it makes no contribution to the NHPT. It is conceptually valid that this simple model can trace the evolution of band structures, as our experimental setting of gain is far above the NHPT critical point. Moreover, considering the inhomogeneous distribution of parametric gains in the lattice, we developed a method based on the nonlinear Schrödinger equation (NLSE) to accurately simulate the static distribution of the light field and the dynamics of the NHPT (see Supplementary Section 3 for details). Note that when the device works in the nonlinear regime, the NH bulk-boundary correspondence[25] is not suitable for domain-wall NH topological insulators due to the absence of periodic gain–loss distributions.

We now focus on the transformation of band structures with an increase of the effective gain ($g\delta L$), where g can be well controlled by external excitation by means of FWM and δL is a quarter of the ring circumference. Figure 2d,e, shows the NHPT taking place in the

bandgap across the exceptional point (EP) at $\epsilon = \pi/T$. With an increase in gain, the topological edge modes at $\epsilon = 0_\pm$, the field distributions of which highly overlap with the gain domain, first possess eigenvalues with imaginary gain (Fig. 2g). They begin to dominate the NHPT process, cross the band of bulk modes and produce two coupled counter-propagating edge modes at the gain–loss junction biased to the loss domain. When the gain is enhanced above the EP, the real parts of energy bands meet at the symmetry point, whereas the imaginary parts split into two separated bands (Fig. 2h). Subsequently, the two gain–loss interface modes become decoupled and they independently reconnect the bandgap, although the one biased to the loss domain tends to be weaker, by contrast (Fig. 2i).

Figure 2f shows a full phase diagram of NH and topological phases for the bandgap at $\epsilon = \pi/T$, when the FTI works in the non-linear regime (the left vertical axis returns to the phase diagram in the linear regime, as shown in Supplementary Fig. 3d). The diagram includes three phases {1, 2 and 3}. We are mainly interested in phase 3, in which the topology and non-Hermiticity mutually interact with each other by means of optical nonlinearity. The topological transport of the pump and signal light in the topological edge modes, together with the prohibition of idler light in the forbidden bandgaps, impose a balance between nonlinearity-induced NH amplification on the edges and dissipation into the bulk, leading to the NHPT of idler light. Importantly, the mutual interactions of topology and non-Hermiticity by means of nonlinearity can lead to a co-beneficial combination, that is, the immunity of imperfections and fast all-optical controllability. That being said, such interplay is the basis of our main result in this

work, which is the demonstration of fast topologically protected NHPT. In comparison, there is no NHPT in regime 2, because all electromagnetic energy is perfectly transported along the connatural topological edges.

The NH phase transition is nonlinearly driven by the FWM. A continuous-wave laser at 1,542.00 nm amplified to 500 mW is used as the pump and another laser tunable over (1,586 nm, 1,590 nm) is used as the signal. The idler produced by FWM is around 1,498 nm. At 1,498 nm, the device originally worked in the forbidden bandgap of the CI phase as $\theta \sim 0.35\pi$ is under the TPT critical point (Fig. 3d). However, as a result of $g\delta L > 0.34$, the FWM gain was above the EP, so that NHPT happened. In the experiment, we collected the FWM-generated idler light in the windows of {idler I, II and III} in Fig. 3c, which, respectively, correspond to the signal in the windows of {signal I, II and III} in Fig. 3e. Figure 3g,i,k shows infrared imaging of the FWM-generated idler in the FTI working in the nonlinear regime. In Fig. 3g(i), the topological edge (bulk) mode transport (dissipates, localizes), with no obvious difference compared with those in the linear regime (Fig. 3f,h). Key results are reported in Fig. 3k. The NHPT takes place from the forbidden bandgap (Fig. 3j) to the NH conducting edge modes (Fig. 3k), at the nonlinearity-driven gain–loss boundary junction in the FTI. Furthermore, the transport of NH edge modes does not follow the 'S'-shaped path any more, which is different from that of the topological edge modes. Note that the presence of noise in Fig. 3k is due to a relatively weak amount of internally generated idler light scattered from the waveguides. The bottom plots in Fig. 3g,i,k show simulated field distributions that are consistent with measured results. Figure 3l shows the measured intensity of the idler, as the NHPT occurs. A high signal-to-noise ratio is observed, which indicates the NHPT from the switch-off forbidden bandgaps (with no signal) to the switch-on transported mode (with signal).

We validate that the reconstructed transport channels on the NH edges remain coherent. Coherence can be directly probed by interferometric measurement. We built a Mach–Zehnder interferometer with the FTI embedded in the middle and measured interference fringes beating between two NH edge modes at the upper and lower boundaries (see experimental set-up in Supplementary Fig. 10). The FTI supports the two NH edge states with identical spectral distributions at the two boundaries[23], which thus allows the interferometric measurement of coherence. The two edges are equally excited. Figure 4 reports contrastive interference fringes which are measured in the FTI in the linear and/or nonlinear regimes. A sequence of interference fringes in the windows of {idler I, II, III}, respectively, were measured and they were grouped to comprehensively portray the coherence properties. Coherence can be quantified by an average fidelity (F) of all fringes. In Fig. 4a,d(b,e), the topological edge (bulk) modes retain (dismiss) coherence, which is implied by the unambiguous constructive (destructive) interference patterns. As shown in Fig. 4c,f, constructive interference fringes emerge from destructive ones and the F reaches a high level of 0.955 ± 0.014. The results confirm that, as the result of NHPTs, coherence-preserved transport channels have been built up at the two gain–loss junctions along the FTI boundaries. In another words, the coherence measurement implies the presence of NH edge modes, instead of modes in bulk or bandgaps. In addition, the unidirectional gain governed by phase-matching in FWM reduces the impact of back-reflection from sidewall roughness.

The FWM allows nearly instantaneous nonlinear responses of the order of picoseconds or femtoseconds[27]. Adoption of the FWM as a highly controllable tool to interact topology and non-Hermiticity promises the realization of a fast operating NHPT. In our dynamic characterization of an NHPT, we modulated the signal light to drive the FTI and probe the idler light that is generated at the gain–loss junction of the NH edges of the FTI (see the experimental set-up in Supplementary Fig. 11). The pump light was fixed. The driving signal and triggering detection system are synchronized with an arbitrary
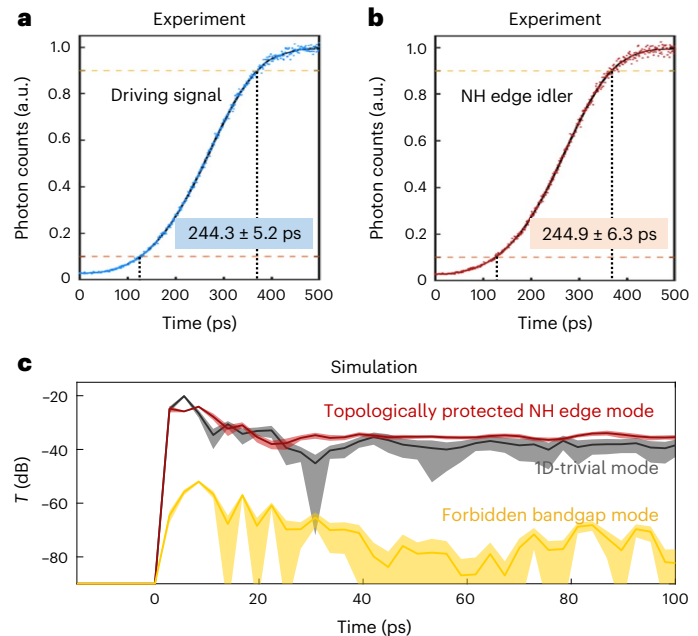
Fig. 5 | Fast topologically protected NH phase transitions. a–c, The signal light is externally launched to drive the FTI, and the internally generated idler light at the gain–loss junction of the FTI is subsequently probed. **a**, Driving signal light, rapidly modulated with a rise time of 244.3 ± 5.2 ps. **b**, Time response of the probed FWM-generated idler light. Fast switching on the signal light (pump is fixed) allows instantaneous amplification of the idler light and switching on of the NH phase on the edge of the FTI. The rise time for the idler light is measured to be 244.9 ± 6.3 ps, which indicates the fast NHPT at the picosecond scale. Both the signal and idler light are attenuated down and then detected by a fast single-photon detector. a.u. indicates normalized single-photon counts are plotted for clarity. Points refer to experimental results and solid lines refer to fitting. The rise time is defined as the time rising from 10% to 90% of the stable maximal photon counts. In **a**,**b**, uncertainties in rise time are estimated from the Poissonian statistics of photons. **c**, Simulated dynamic evolution of the fast NHPT. The dynamics of NH edge modes (red) converge within 15 ps, which implies the theoretical limit of NHPT in the lattice. The dynamics for the forbidden bandgaps in the FTI (yellow) and the trivial mode in a 1D array of microrings (grey) are plotted for comparison. Error bars for topological devices are considerably smaller than those for trivial devices. As the statistical analysis shows, the NH edge mode throughout the fast NHPT is topologically protected against disorders, whereas the trivial mode in the 1D microrings lacks such immunity. A set of 50 samples with random disorders are used in the simulation. In **c**, shaded areas represent $\pm 3\sigma$ uncertainty and solid lines are the mean.

waveform generator. Light was attenuated and detected by a fast single-photon detector with a 50 ps jitter. Figure 5b shows the measured time response of the idler light, using the driving signal as a reference plot in Fig. 5a. The rise time of the signal (driving) light and the idler (probed) light in NH edges were measured to be 244.3 ± 5.2 ps and 244.9 ± 6.3 ps, respectively. Experimental results thus confirm the picosecond-scale switching of NH phase transitions. We developed the NLSE model to simulate the dynamic evolution of a nonlinearity-driven NHPT in the lattice. Figure 5c shows the simulated time dynamics of the NHPT, and the field distributions at different time steps are provided in Supplementary Fig. 7. The theoretical limit of the convergence time of the NHPT is estimated to be less than 20 ps, which is determined by the balance of inhomogeneous light amplification and light interference in the lattice. In our measurements, the speed of NH topological switching was limited by the bandwidth of the electronic system. With more dedicated electronic control and measurement, faster phase transitions are achievable making it comparable with standard optical switching devices in silicon[52].

An intriguing feature of photonic topological insulators is robustness against certain imperfections, which has been observed in a variety of photonic devices[2–12,20–23]. Here, we further show that the fast optical switching devices can be topologically protected. In the linear regime, the FTI possesses robust light transport along the boundaries of the domain wall, when fabrication disorders are present (see the experimental results for a fabricated device in Fig. 3a,f and simulation results in Supplementary Fig. 8). In contrast, the one-dimensional (1D) array of microrings lacks such immunity against disorders (Supplementary Fig. 8). Importantly, robustness can be inherited from the externally input pump and/or signal in the topological edge modes to the internally generated idler light in the NH edge modes. In the nonlinear regime, using the NLSE, we numerically simulate the static field distribution and NHPT dynamics in disordered FTIs. Figure 3k shows a simulation of the static distribution in the FTI with disorders of coupling strengths and phases, which is consistent with the experimental results for the device with fabrication disorders. Such topological protection penetrates the whole dynamic evolution of the fast NHPT, as shown in Fig. 5c. The dynamics for trivial modes and forbidden bandgaps are shown for comparison. A slight variation of light transport is observed in the NH edge modes through the NHPT, compared with the trivial 1D device. The immunity against deliberately induced structure defects is numerically confirmed in the FTIs in linear and nonlinear regimes.

We have observed the topologically protected fast manipulation of NH phase transitions in the photonic FTI, driven by strong optical nonlinearities in passive silicon nanophotonic devices. These findings show a highly controllable way of bridging topology and NH physics using nonlinearities. It may allow further understanding of complex multiple phase transitions and collective phenomena, emergence of correlated states and emulations of condensed matter, high energy physics and quantum open systems. It also provides a route towards new designs of robust photonic devices for practical applications, such as high-speed optical switching and modulation, wavelength conversion, parametric amplification and signal regeneration for optical information processing, telecommunications and interconnection[38], and quantum information processing and communication[39]. Nonlinearities, which commonly exist in optical materials and are generally in electronic, mechanical and atomic systems, may provide a means for fast control of robust topological NH devices for potential classical and quantum applications.

Online content

Any methods, additional references, Nature Portfolio reporting summaries, source data, extended data, supplementary information, acknowledgements, peer review information; details of author contributions and competing interests; and statements of data and code availability are available at https://doi.org/10.1038/s41567-023-02244-8.

References

1. Hasan, M. Z. & Kane, C. L. Colloquium: topological insulators. *Rev. Mod. Phys.* **82**, 3045–3067 (2010).
2. Haldane, F. D. M. & Raghu, S. Possible realization of directional optical waveguides in photonic crystals with broken time-reversal symmetry. *Phys. Rev. Lett.* **100**, 013904 (2008).
3. Wang, Z. et al. Observation of unidirectional backscattering-immune topological electromagnetic states. *Nature* **461**, 772–775 (2009).
4. Lu, L., Joannopoulos, J. D. & Soljačić, M. Topological photonics. *Nat. Photon.* **8**, 821–829 (2014).
5. Ozawa, T. et al. Topological photonics. *Rev. Mod. Phys.* **91**, 015006 (2019).
6. Khanikaev, A. B. & Shvets, G. Two-dimensional topological photonics. *Nat. Photon.* **11**, 763–773 (2017).
7. Rechtsman, M. C. et al. Photonic Floquet topological insulators. *Nature* **496**, 196–200 (2013).
8. Maczewsky, L. J. et al. Observation of photonic anomalous Floquet topological insulators. *Nat. Commun.* **8**, 13756 (2017).
9. Hafezi, M. et al. Robust optical delay lines with topological protection. *Nat. Phys.* **7**, 907–912 (2011).
10. Hafezi, M. et al. Imaging topological edge states in silicon photonics. *Nat. Photon.* **7**, 1001–1005 (2013).
11. Dong, J.-W. et al. Valley photonic crystals for control of spin and topology. *Nat. Mater.* **16**, 298–302 (2017).
12. Shalaev, M. I. et al. Robust topologically protected transport in photonic crystals at telecommunication wavelengths. *Nat. Nanotechnol.* **14**, 31–34 (2019).
13. Bender, C. M. & Boettcher, S. Real spectra in non-Hermitian Hamiltonians having pt symmetry. *Phys. Rev. Lett.* **80**, 5243 (1998).
14. El-Ganainy, R. et al. Non-Hermitian physics and pt symmetry. *Nat. Phys.* **14**, 11–19 (2018).
15. Feng, L., El-Ganainy, R. & Ge, L. Non-Hermitian photonics based on parity–time symmetry. *Nat. Photon.* **11**, 752–762 (2017).
16. Özdemir, Ş. K. et al. Parity–time symmetry and exceptional points in photonics. *Nat. Mater.* **18**, 783–798 (2019).
17. Weidemann, S. et al. Topological triple phase transition in non-Hermitian Floquet quasicrystals. *Nature* **601**, 354–359 (2022).
18. Zhao, H. et al. Non-Hermitian topological light steering. *Science* **365**, 1163–1166 (2019).
19. Ao, Y. et al. Topological phase transition in the non-Hermitian coupled resonator array. *Phys. Rev. Lett.* **125**, 013902 (2020).
20. Bandres, M. A. et al. Topological insulator laser: experiments. *Science* **359**, eaar4005 (2018).
21. Mittal, S., Goldschmidt, E. A. & Hafezi, M. A topological source of quantum light. *Nature* **561**, 502–506 (2018).
22. Blanco-Redondo, A. et al. Topological protection of biphoton states. *Science* **362**, 568–571 (2018).
23. Dai, T. et al. Topologically protected quantum entanglement emitters. *Nat. Photon.* **16**, 248–257 (2022).
24. Weimann, S. et al. Topologically protected bound states in photonic parity–time-symmetric crystals. *Nat. Mater* **16**, 433–438 (2017).
25. Xiao, L. Non-Hermitian bulk-boundary correspondence in quantum dynamics. *Nat. Phys* **16**, 761–766 (2020).
26. Wang, K. et al. Generating arbitrary topological windings of a non-Hermitian band. *Science* **371**, 1240–1245 (2021).
27. Boyd, R. W. *Nonlinear Optics* 2nd edn (Academic Press, 2008).
28. Smirnova, D. et al. Nonlinear topological photonics. *Appl. Phys. Rev.* **7**, 021306 (2020).
29. Maczewsky, L. J. et al. Nonlinearity-induced photonic topological insulator. *Science* **370**, 701–704 (2020).
30. Kruk, S. et al. Nonlinear light generation in topological nanostructures. *Nat. Nanotechnol.* **14**, 126–130 (2019).
31. Hu, Z. et al. Nonlinear control of photonic higher-order topological bound states in the continuum. *Light Sci. Appl.* **10**, 1–10 (2021).
32. Kirsch, M. S. et al. Nonlinear second-order photonic topological insulators. *Nat. Phys.* **17**, 995–1000 (2021).
33. Mukherjee, S. & Rechtsman, M. C. Observation of Floquet solitons in a topological bandgap. *Science* **368**, 856–859 (2020).
34. Konotop, V. V., Yang, J. & Zezyulin, D. A. Nonlinear waves in PT-symmetric systems. *Rev. Mod. Phys.* **88**, 035002 (2016).
35. Rüter, C. E. et al. Observation of parity–time symmetry in optics. *Nat. Phys.* **6**, 192–195 (2010).
36. Lumer, Y. et al. Nonlinearly induced *PT* transition in photonic systems. *Phys. Rev. Lett.* **111**, 263901 (2013).
37. Xia, S. et al. Nonlinear tuning of PT symmetry and non-Hermitian topological states. *Science* **372**, 72–76 (2021).

38. Minzioni, P. et al. Roadmap on all-optical processing. *J. Opt.* **21**, 063001 (2019).

39. Wang, J. et al. Integrated photonic quantum technologies. *Nat. Photon.* **14**, 273–284 (2020).

40. Zeljkovic, I. et al. Strain engineering Dirac surface states in heteroepitaxial topological crystalline insulator thin films. *Nat. Nanotechnol.* **10**, 849–853 (2015).

41. Kudyshev, Z. A. et al. Photonic topological phase transition on demand. *Nanophotonics* **8**, 1349–1356 (2019).

42. Cheng, X. et al. Robust reconfigurable electromagnetic pathways within a photonic topological insulator. *Nat. Mater.* **15**, 542–548 (2016).

43. Leykam, D. et al. Reconfigurable topological phases in next-nearest-neighbor coupled resonator lattices. *Phys. Rev. Lett.* **121**, 023901 (2018).

44. Shalaev, M. I., Walasik, W. & Litchinitser, N. M. Optically tunable topological photonic crystal. *Optica* **6**, 839–844 (2019).

45. You, J. W. et al. Reprogrammable plasmonic topological insulators with ultrafast control. *Nat. Commun.* **12**, 5468 (2021).

46. Rudner, M. S. et al. Anomalous edge states and the bulk-edge correspondence for periodically driven two-dimensional systems. *Phys. Rev. X* **3**, 031005 (2013).

47. Kitagawa, T. et al. Topological characterization of periodically driven quantum systems. *Phys. Rev. B* **82**, 235114 (2010).

48. Liang, G. Q. & Chong, Y. D. Optical resonator analog of a two-dimensional topological insulator. *Phys. Rev. Lett.* **110**, 203904 (2013).

49. Afzal, S. et al. Realization of anomalous floquet insulators in strongly coupled nanophotonic lattices. *Phys. Rev. Lett.* **124**, 253601 (2020).

50. Guglielmon, J. et al. Photonic realization of a transition to a strongly driven Floquet topological phase. *Phys. Rev. A* **97**, 031801 (2018).

51. Foster, M. A. et al. Broad-band optical parametric gain on a silicon photonic chip. *Nature* **441**, 960–963 (2006).

52. Lipson, M. The revolution of silicon photonics. *Nat. Mat.* **21**, 974–975 (2022).

Author contributions

T.D. and J.W. conceived the project. T.D., J.M., Y.Y., Y.Z., C.Z. and B.T. implemented the experiment. T.D. provided the simulations and performed the theoretical analysis. T.D., Y.A., Y.L. and J.Y. discussed and improved the theoretical results. Z.L., J.L., W.W., X.H., Q.G. and J.W. managed the project. T.D. and J.W. wrote the manuscript with input from all the authors. All the authors discussed the results and contributed to the manuscript.

Competing interests

The authors declare no competing interests.

Additional information

Supplementary information The online version contains supplementary material available at https://doi.org/10.1038/s41567-023-02244-8.

Correspondence and requests for materials should be addressed to Jianwei Wang.

Peer review information *Nature Physics* thanks Jiangbin Gong and the other anonymous reviewer(s) for their contribution to the peer review of this work.

Reprints and permissions information is available at www.nature.com/reprints.